ELSEVIER

Contents lists available at ScienceDirect

## Sensors and Actuators Reports

journal homepage: www.elsevier.com/locate/snr



# A high-temperature heat flux sensor using the transverse Seebeck effect in elemental rhenium

Kenneth McAfee a, Peter B. Sunderland b, Oded Rabin c,d,\*

- <sup>a</sup> Department of Aerospace Engineering, University of Maryland, College Park, MD 20742, USA
- <sup>b</sup> Department of Fire Protection Engineering, University of Maryland, College Park, MD 20742, USA
- <sup>c</sup> Department of Materials Science and Engineering, University of Maryland, College Park, MD 20742, USA
- d Institute for Research in Electronics and Applied Physics, University of Maryland, College Park, MD 20742, USA

#### ARTICLE INFO

#### Keywords: Transverse thermoelectric Heat flux sensor Refractory metal Single crystal Sensor calibration

## ABSTRACT

Heat flux sensors compatible with hot environments are critical to advance aerospace, materials, and energy generation technologies that cope with extreme thermal conditions. In this work, we report on the development and characterization of a high-temperature heat flux sensor using the transverse Seebeck effect in rhenium single crystals. The sensor leverages refractory alloys and ceramics compatible with temperatures exceeding 1000 °C. The heat flux sensor was characterized from room temperature to 500 °C using a temperature-controlled calibration facility. At constant temperature, the sensor's voltage output is linear with respect to the absorbed heat flux. The responsivity of the sensor varies with temperature, from 1.3  $\mu$ V/(W/cm²) at room temperature to  $-3.2 \mu$ V/(W/cm²) at 500 °C, increasing monotonically in magnitude after changing sign positive to negative at approximately 300 °C. The experimental results are in good agreement with analytical predictions of the sensor's temperature-dependent responsivity, which suggest a further increase in magnitude up to  $-7.4 \mu$ V/(W/cm²) at 1000 °C. These results highlight the unique characteristics of rhenium as a TSE transducer. The design offers compatibility with a wide range of operating temperatures and yields a measurement sensitivity that increases as the environmental conditions become more challenging.

## 1. Introduction

Heat flux measurements in extreme environments are critical to study high-temperature flow phenomena, evaluate the performance of thermal protection systems, and monitor system health. In applications such as high-speed flight, materials production, combustion, and energy generation, heat flux sensors must contend with temperatures ranging from 500 °C to over 1000 °C [1–3]. Typical heat flux sensors are, however, often limited by low maximum operational temperatures (< 200 °C) and require active or passive cooling infrastructure embedded in the surrounding structure [4–6]. These limitations have motivated the recent development of heat flux sensors better suited for extreme environment applications.

Sensors developed for extreme environments have most commonly leveraged high-temperature thermoelectric materials in thermopile configurations. In these devices, a temperature difference is induced between multiple bi-metal junctions, producing a thermoelectric voltage via the conventional Seebeck effect (CSE) [7]. Originally, this mechanism was exploited in sensors using type-K thermocouple materials to achieve maximum operational temperatures up to  $1000\ ^{\circ}\text{C}\ [8-10]$ .

Since then, other high-temperature thermopile sensors have been reported on, including those using type-N [11,12], type-S [13], and type-C [14] thermocouple materials to achieve operational temperatures in excess of 850 °C. Thermopile-type sensors, however, often exhibit complex constructions and many single points of failure. These caveats are intrinsic to the sensor mechanism of operation, which requires many serial junctions between dissimilar thermoelectric materials, with half of the junctions located on the hot side of the sensor.

The transverse Seebeck effect (TSE) has been explored as an alternative transduction mechanism to measure heat flux in a ruggedized sensor package [15,16], with more recent work demonstrating the mechanism at high temperatures [17,18]. The TSE is a phenomenon that arises in anisotropic thermoelectric materials, whereby an induced temperature gradient generates an orthogonal voltage [19,20]. Devices using the TSE only require a single transducer material to generate a voltage output, in contrast with a pair of materials required for thermopile sensors. Furthermore, all electrical wire connections can be integrated on the cold side of the transducer, avoiding the placement of any weld or solder joints near the hottest portions of the sensor.

<sup>\*</sup> Corresponding author.

E-mail address: oded@umd.edu (O. Rabin).

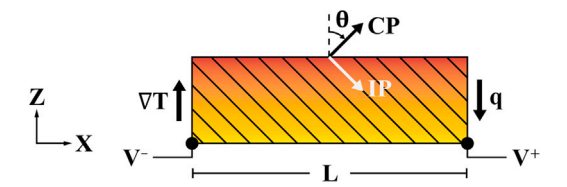


Fig. 1. Schematic of the transverse Seebeck effect in an anisotropic single crystal. A voltage is generated between two probe locations separated by a distance L along the x-direction in response to a temperature gradient induced along the z-direction. In the schematic, CP and IP represent the cross-plane and in-plane crystal orientations, respectively, and  $\theta$  represents the relative tilt between the coordinate systems defined by the crystal structure and the transducer geometry.

Generally, heat flux sensors using the TSE exhibit more robust constructions compared with their thermopile counterparts, yielding good compatibility with extreme environments.

Heat flux sensors utilizing the TSE have leveraged textured thin films, layered composites, and anisotropic single crystals. Thin films have been investigated for high-speed sensing applications due to the large temporal bandwidth that can be achieved by reducing the thickness of the transducer to the sub-micrometer scale. These sensors have predominantly leveraged YBa<sub>2</sub>Cu<sub>3</sub>O<sub>7-d</sub> [21–28] and other oxides [29–31], with recent advances extending the technology toward high-temperature applications (up to 1000 °C) via La<sub>1-x</sub>Ca<sub>x</sub>MnO<sub>3</sub> thin films [18].

In larger form-factor sensors, layered composite TSE transducers, such as those using Chromel/Alumel [16] and nickel/stainless steel [32, 33] material combinations, have been utilized to achieve operating temperatures up to 600 °C; special care, however, must be taken to avoid interdiffusion of adjacent layers, which can cause drifts in sensor characteristics, notably at high temperatures. Similar to thin films, single crystals have been investigated extensively for TSE-based sensors, with prior art including sensors using single crystal antimony [15], bismuth [34,35], and Bi<sub>2</sub>Te<sub>3</sub> [36]. These studies have predominantly focused on highly anisotropic single crystals which yield large responsivities at room temperature, however, recent contributions investigating TSE-based sensors using crystalline 4H-SiC have demonstrated good compatibility of the transducer platform with temperatures as high as 800 °C [17,37].

In this work, the TSE in single crystal rhenium is demonstrated as a viable transduction mechanism in a robust heat flux sensor tailored for hot environments. The responsivity of the sensor is characterized at application-relevant temperatures and compared with predictions using as-built device parameters and literature-based transport properties. The transient response of the sensor is evaluated subject to dynamic heating conditions. Lastly, the relative contributions of the TSE and CSE in the sensor are investigated using a laser scan technique [15].

## 2. Sensor operating mechanism

The TSE, illustrated schematically in Fig. 1, occurs in an anisotropic single crystal when the principal crystallographic axes are tilted with respect to the direction of an induced temperature gradient. Assuming a uniform temperature gradient in the z-direction in Fig. 1, the voltage generated along the x-direction due to the TSE is given by [23]

$$V_x = q_z \frac{S_{CP} - S_{IP}}{k} L \sin \theta \cos \theta \tag{1}$$

In Eq. (1),  $S_{IP}$  and  $S_{CP}$  are the in-plane (IP) and cross-plane (CP) components of the anisotropic Seebeck coefficient tensor, respectively,  $\theta$  is the inclination of the CP orientation (corresponding to  $\langle 0001 \rangle$  in Miller-Bravais notation) from the *z*-axis towards the *x*-axis (Fig. 1), and k is the thermal conductivity (assumed isotropic in rhenium [38]). The

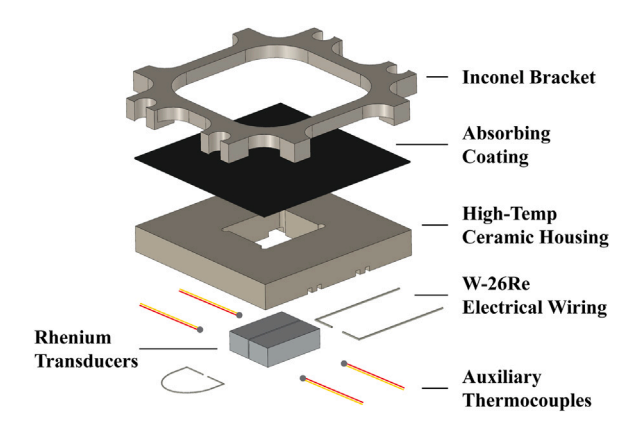


**Fig. 2.** Exploded view of the high-temperature TSE heat flux sensor. Two rhenium transducers are connected in series using tungsten-rhenium alloy electrical wiring and mounted in a ceramic package. Four auxiliary thermocouples monitor the temperature near each transducer and electrical wire junction. The front face of the sensor is coated with a high absorptivity paint. An Inconel bracket is placed over the front of the sensor for mounting to a heat sink.

parameter L is the length of the transducer along the x-direction, or cumulative length of all transducers if multiple are wired in series [15, 39]. The parameter  $q_z$  is the heat flux parallel to the z-axis and is related to the temperature gradient  $\partial T/\partial z$  via Fourier's law (Eq. (2)).

$$q_z = -k\frac{\partial T}{\partial z} \tag{2}$$

## 3. Heat flux sensor design and fabrication

The high-temperature TSE heat flux sensor, shown in Fig. 2, consists of two prismatic rhenium transducers, electrical wiring, a ceramic housing, and four auxiliary thermocouples. All components were fabricated using alloys and ceramics with maximum operating temperatures exceeding 1000 °C. The two prismatic single crystals of elemental rhenium (Princeton Scientific), measuring  $5.3 \times 2.1 \times 1.3$  mm (L × W × H) and with a crystal inclination of  $\theta = -\pi/4$  (following the convention in Fig. 1), were secured in the ceramic housing (Aremco Aremcolox Bisque-Fired Alumina 96%) using cement (Sauereisen Tempseal No. 3) (Fig. 3). Tungsten-rhenium alloy wires (Omega Engineering W-26Re, 0.25 mm diameter) were spot-welded on the back-side of the rhenium transducers, towards the heat sink. Four auxiliary type-K thermocouples (Omega Engineering model 5SRTC-GG-K-30-36-ROHS) were embedded in the sensor near each transducer and electrical wire junction (Fig. 3). The front face of the sensor, facing the heat source, was spray-coated with high-temperature black paint (Rust-Oleum model 248903). Following fabrication, the sensor was baked at 300 °C for approximately 1 h to fully cure the black paint. To avoid adhesives, a front-side bracket (McMaster-Carr, Alloy X) and screws were used to secure the sensor to a heat sink (Fig. 4). The complete sensor has a frontal area of 196 mm<sup>2</sup> and a thickness of 2.1 mm. The two rhenium transducers are connected in series, augmenting the sensor response with a cumulative length of 8.3 mm between welded electrical contacts (out of a combined transducer length of 10.6 mm). The sensor's voltage signal is collected by connecting the tungstenrhenium electrical wires to the terminals of a nanovoltmeter (Keithley model 2182A). The auxiliary thermocouples were connected to a data acquisition module (Pico Technology TC-08).

## 4. Predicted responsivity

Eq. (1) provides a means for modeling the responsivity  $C_{TSE}$  of the TSE heat flux sensor when the thermoelectric properties of the transducer material are known. Defining the sensor responsivity as the

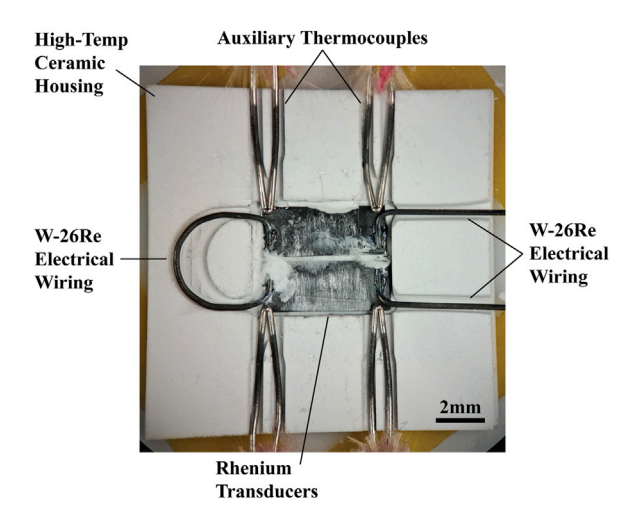


**Fig. 3.** Optical image of the back side of the TSE heat flux sensor during assembly, prior to sealing with cement. Visible components include the two transducers, electrical wiring, and thermocouples. Scale bar: 2 mm.

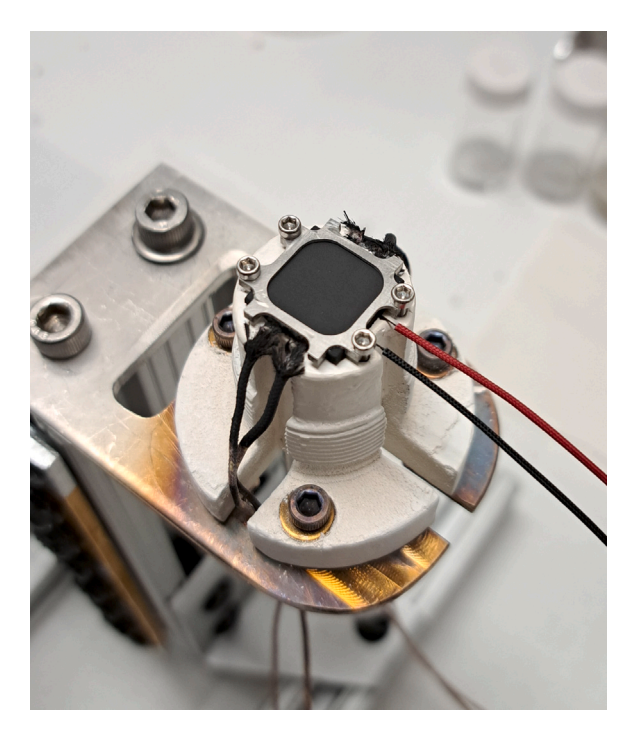


**Fig. 4.** High-temperature TSE heat flux sensor mounted to a copper heat sink. The heat sink is spray-coated with boron nitride to inhibit oxidation. The heat sink has integrated coolant channels for water or air (not visible).

ratio between the measured voltage  $V_x$  and the heat flux absorbed by the front face  $-q_z$ ,

$$C_{TSE} = -\frac{V_x}{q_z} = -\frac{S_{CP} - S_{IP}}{k} L \sin \theta \cos \theta$$
 (3)

In rhenium, the Seebeck coefficient anisotropy  $\Delta S = S_{CP} - S_{IP}$  varies with temperature, decreasing from a value of 1.5 µV/K at 25 °C to 0 µV/K at 275 °C, and then to -8.3 µV/K at 1000 °C [40]. Between 300 °C and 1000 °C, the Seebeck coefficient anisotropy decreases (increases in magnitude) linearly with increasing temperature. Over the same temperature range, the thermal conductivity (assumed nearly isotropic) varies little, betweeen 0.44 and 0.48 W/cm-K [41]. The Seebeck coefficient anisotropy and thermal conductivity of rhenium are shown in Fig. 5, normalized by their value at 25 °C,  $\Delta S_0$  and  $k_0$ ,

Table 1
Uncertainty bounds for the parameters in Eq. (3).

Parameter $(\chi_i)$	Uncertainty $(\sigma_{\chi_i})$	Reference
$S_{IP}, S_{CP}$	$\pm$ 0.5 $\mu$ V/K	[42]
k	$\pm$ 5% (T < 200 °C) or $\pm$ 15% (T >= 200 °C)	[41]
$\theta$	$\pm \pi/180$	This work
L	± 0.1 mm	This work

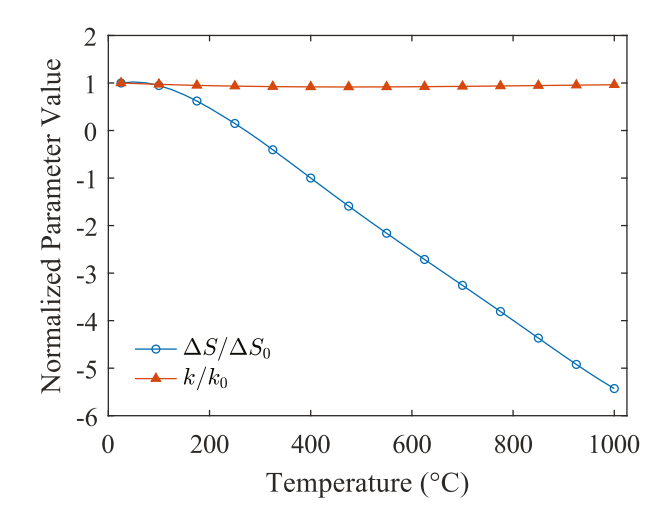


**Fig. 5.** Thermoelectric transport properties of rhenium. The Seebeck coefficient anisotropy  $\Delta S = S_{CP} - S_{IP}$  [40] and thermal conductivity k [41] are shown relative to their value at 25 °C,  $\Delta S_0$  and  $k_0$ , respectively.

respectively. Fig. 5 illustrates that the temperature-dependence of the predicted responsivity of the TSE heat flux sensor is dominated by the temperature-dependence of  $\Delta S$  in rhenium. Applying Eq. (3) to the asbuilt heat flux sensor, with an effective transducer length of 8.3 mm and an inclination of  $-\pi/4$ , the responsivity of the sensor, shown in Fig. 6, is predicted to be 1.3  $\mu$ V/(W/cm²) at 25 °C, decreasing in value to  $-7.4~\mu$ V/(W/cm²) at 1000 °C, and changing sign from positive to negative at 275 °C.

The uncertainty of the predicted responsivity was estimated to establish upper and lower bounds for comparison against experimental calibration results (Section 5). The total uncertainty  $\sigma_t$  is calculated by propagating the uncertainties of each parameter  $\chi_i$  in Eq. (3) via a root-sum-square

$$\sigma_t = \sqrt{\sum_{i=1}^{5} \left[ \frac{\partial C_{TSE}}{\partial \chi_i} \sigma_{\chi_i} \right]^2} \tag{4}$$

Uncertainty bounds for the five parameters in Eq. (3) are tabulated in Table 1, where each parameter is assumed to be normally distributed about its mean value. The upper and lower bounds of the predicted temperature-dependent responsivity, representing the nominal value of  $C_{TSE} \pm 1\sigma_t$ , are shown in Fig. 6.

## 5. Temperature-dependent sensor calibration

The responsivity of the TSE heat flux sensor was characterized from room temperature to  $500\,^{\circ}\text{C}$  repeatedly over a period of 9 months, during which the sensor was exposed to temperatures ranging from  $20\,^{\circ}\text{C}$  to  $1000\,^{\circ}\text{C}$ . Calibrations were performed using a high-temperature calibration facility. The facility, detailed in [43], uses a transfer calibration technique, where the output of the TSE heat flux sensor is compared to that of a reference Schmidt-Boelter heat flux sensor (Medtherm model 64P-25SB-24K, serial number 234941) with the two exposed to an identical heat flux [15,44,45]. The temperature of the TSE heat

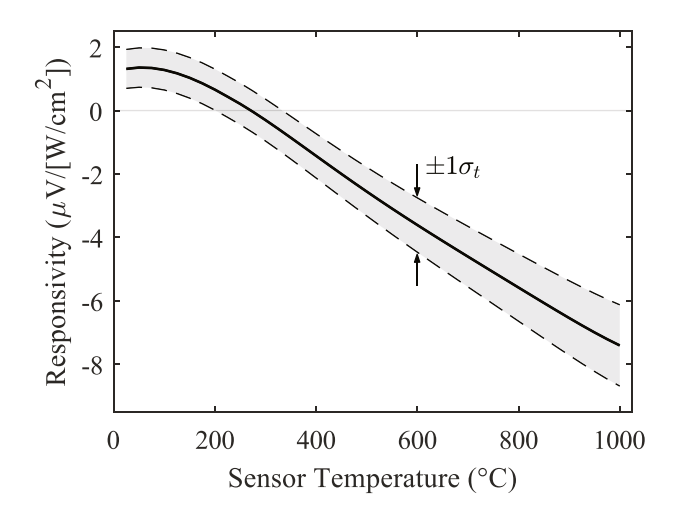


**Fig. 6.** Predicted responsivity  $C_{TSE}$  of the TSE heat flux sensor from Eq. (3) (solid line). The dashed lines represent upper and lower bounds for the predicted responsivity due to the uncertainties of the parameters in Eq. (3). The shaded region bounded by the dashed lines captures responsivity values that are within 1 standard deviation of the nominal prediction.

flux sensor is modulated using a PID-controlled cylindrical band heater while the reference sensor is maintained at room temperature using cooling water. At temperatures above 350 °C, the sensor is maintained under industrial grade nitrogen gas, and above 520 °C under ultra high purity argon. An adjustable high-output infrared lamp (Precision Control Systems Inc. StripIR 5306B, 1000 W) is used to generate varying levels of heat flux. When exposed to the infrared lamp, the TSE heat flux sensor is maintained at a steady temperature, as measured by the auxiliary thermocouples, by controlling the power to the band heater. An additional water-cooled reference plate is used to provide the TSE heat flux sensor with a stable baseline heating condition when positioned out of the line-of-sight of the infrared lamp. The facility can perform accurate calibrations of heat flux sensors from room temperature to 500 °C and, notably, can maintain the sensor temperature to within 1% of the target set point value when exposed to different levels of heat flux.

For each set point temperature, a response curve (voltage vs. heat flux) was generated by exposing both sensors sequentially to four different heat fluxes ranging from 0.5 to 2.5 W/cm². Heat fluxes were calculated from the reference sensor voltage using the manufacturer-supplied response curve. For each heat flux, the TSE heat flux sensor voltage was taken as the difference in the steady-state output signal between when the sensor is in the line-of-sight of the infrared lamp and when it is positioned in front of the water-cooled reference plate; by comparing the two states, the output signal due to the exposure to the infrared lamp is isolated. Response curves for the six sensor temperatures (referred to hereafter as a *calibration sweep*) are shown in Fig. 7. Over the tested sensor temperature range, the response is linear from 0 to 2.5 W/cm². The slope of a line fit to each set of calibration data yields the temperature-specific responsivity of the TSE heat flux sensor.

The responsivity of the sensor as a function of temperature is shown in Fig. 8a for three calibration sweeps. During the initial calibration sweep, the TSE heat flux sensor exhibited a room temperature responsivity of 1.3  $\mu V/(W/cm^2)$  and a responsivity of  $-3.2~\mu V/(W/cm^2)$  at 500 °C, decreasing monotonically with increasing temperature. In the second sweep, a global decrease in the responsivity of the sensor was observed. During the third sweep, the responsivity of the sensor remained unchanged from the second sweep, indicating that the sensor was stable thereafter.

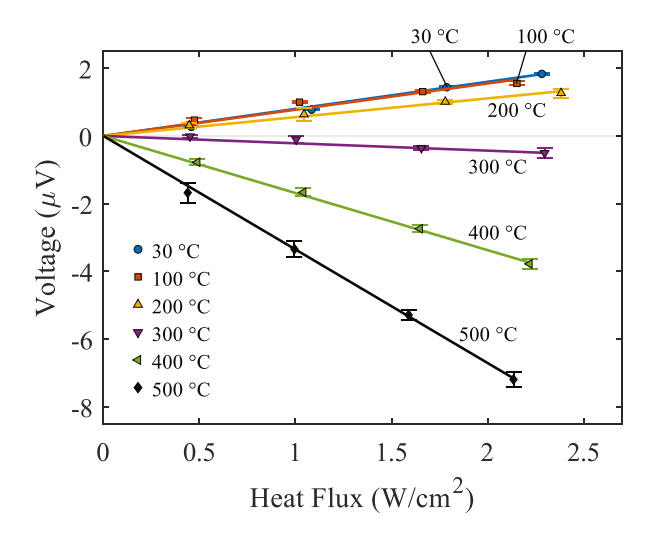


**Fig. 7.** TSE heat flux sensor calibration sweep from room temperature to 500 °C. Error bars represent the uncertainty of the voltage measurement multiplied by a coverage factor of 2 ( $\pm 2\sigma$ ).

To test the resilience of the device, the sensor was heat treated for 10 hrs at 1000 °C in a tube furnace under flow of ultra high purity argon. Diagnostic tests found no changes in the electronic circuit of the sensor. The only impact of the heat treating process on the sensor components was the appearance of cracks in the black paint coating. Since the cracks have the potential to change the emissivity of the sensor, a new coat of paint was applied before a calibration sweep was performed post-heat treatment. Fig. 8b compares the responsivity of the TSE heat flux sensor before and after the heat treatment. The two datasets are consistent with each other. This indicates that the device as a whole, not only the individual components, is compatible with extreme temperatures, at least up to 1000 °C.

## 5.1. Analysis of the sensor's temperature-dependent responsivity

In general, the trend of the measured responsivity with increasing temperature is consistent with predictions from Section 4, with good quantitative agreement during the first calibration sweep for temperatures up to 400 °C. All calibrations, considering a 95% confidence interval, were within the  $\pm$  1 $\sigma_{t}$  uncertainty bounds of the predicted responsivity. In the latter two sweeps, the measured responsivity values become, overall, more negatively biased than the nominal predictions. This behavior is explained next by considering the contributions of the CSE to the output voltage.

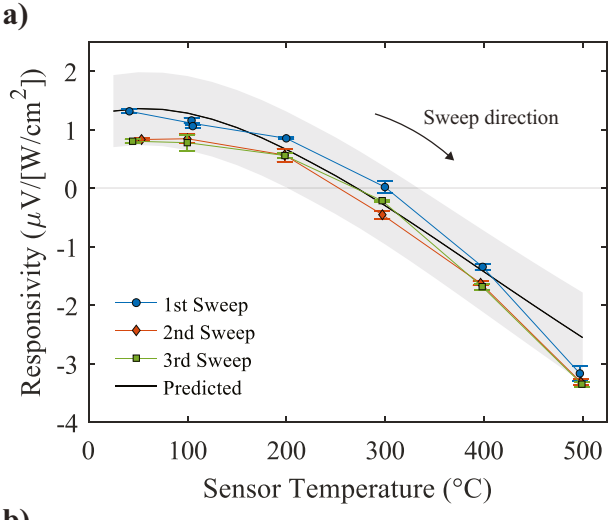
In the calculation of the predicted responsivity (Eq. (3)), it was assumed that the temperature gradient within the transducers was uniform and oriented in the z-direction. This is rarely achieved in practice, as any structural asymmetry, due to variations in the cement thickness, for example, will introduce non-uniform lateral temperature variations in the transducers. These lateral temperature variations may lead to CSE contributions in the output voltage. For two transducers connected in series and arranged such that their crystal orientations are symmetric with respect to a 2-fold rotation about the z-axis (Fig. 9), the CSE voltage  $V_{CSE}$  is proportional to the net temperature difference between the ends of the transducers  $\Delta T_L$ 

$$V_{CSE} = -(S_{IP}\cos^2\theta + S_{CP}\sin^2\theta - S_{wire})\Delta T_L$$
 (5)

where

$$\Delta T_L = (T_4 - T_3) - (T_1 - T_2) \tag{6}$$

In Eq. (5),  $S_{wire}$  represents the Seebeck coefficient of the tungstenrhenium alloy wires, measured to be  $-0.8~\mu V/K$  at room temperature.



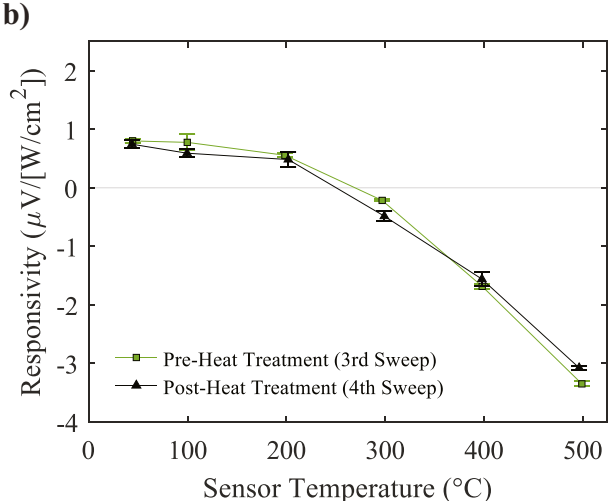


**Fig. 8.** Temperature-dependent sensor responsivity. a) Responsivity from a sequence of calibration sweeps. Error bars represent a 95% confidence interval. The predicted responsivity from Fig. 6 is overlaid on the data for comparison. The shaded region represents responsivity values that fall within the  $\pm 1\sigma_r$  uncertainty bounds of the predicted responsivity. b) Calibration sweeps performed before and after the heat treatment at 1000 °C.

In Eq. (6),  $T_1$  through  $T_4$  are the temperatures of the transducer and electrical wire junctions, as labeled in Fig. 9. The value of  $\Delta T_L$  was estimated using measurements from the four auxiliary thermocouples embedded near each transducer and electrical wire junction (Fig. 3). For each calibration, the trend of  $\Delta T_L$  was linear with respect to the absorbed heat flux. In the first calibration sweep, the value of  $\Delta T_L$ was between -0.38 and -0.3 °C per 1 W/cm2 of absorbed heat flux, except at 500 °C. During the calibration at 500 °C, the value of  $\Delta T_L$ decreased to -0.54 °C per 1 W/cm<sup>2</sup> of absorbed heat flux. The large change in  $\Delta T_L$  was attributed to the settling of sensor components in the package. Throughout the second and third sweeps, the value of  $\Delta T_L$  remained between -0.54 and -0.38 °C per 1 W/cm<sup>2</sup> of absorbed heat flux, indicating that the changes associated with use of the sensor at application-relevant temperatures are complete after less than 1 h. From Eq. (5), it is anticipated that a decrease in  $\Delta T_L$  will lead to a value of  $V_{CSE}$  that is more negative, decreasing the total voltage. This trend is reflected in the results shown in Fig. 8a, where all temperaturespecific responsivity values following the first calibration at 500 °C are more negatively biased versus earlier data and, generally, the nominal predictions. Furthermore, the timing of the decrease of  $\Delta T_L$ provides a reasonable explanation as to why the responsivity at 500 °C

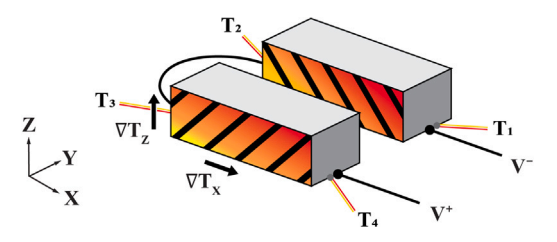


**Fig. 9.** Schematic of the transducer circuit subject to both z- and x-oriented temperature gradients. The net temperature difference between the ends of the transducers  $\Delta T_L$  is estimated using measurements from the four auxiliary thermocouples embedded in the package. The hash marks represent the orientations of the (0001) basal planes in each transducer prism.

changed less from the first sweep to the second sweep versus all other temperatures; during the first 500  $^{\circ}$ C calibration, the measured voltage already included the altered CSE voltage contributions.

#### 6. Transient response

The transient response of the TSE heat flux sensor was investigated at room temperature subject to dynamic heating conditions. The sensor's time response was recorded for multiple heating scenarios, including a step change in heat flux and a sweep of sinusoidal heat flux profiles with varying frequencies. The former measurement was used to determine the characteristic time constant of the sensor [13,26,46]. The latter set of measurements were used to characterize the bandwidth of the sensor via its amplitude-frequency response [23,24].

## 6.1. Step heat flux

The response of the TSE heat flux sensor was characterized subject to a step change in heat flux. A 808 nm continuous-wave diode laser (Thorlabs model L808P500MM) with a  $5\times 5$  mm square beam positioned over the centroid of the sensor was used as the heat source. To generate the heat flux step, the optical power of the laser was modulated between 0 and 144 mW as a square waveform with a frequency of 0.05 Hz. The sensor's voltage was amplified by a factor of 1,000 using a nanovoltmeter (Keithley model 2182) and output to a digital oscilloscope (Pico Technology Picoscope) where it was recorded at 300 Hz. A beam splitter was used to divert 10% of the laser power to a photodiode sensor to detect the onset of each heat flux step.

A total of 36 step transients were recorded for the TSE heat flux sensor. All transients were synchronized and averaged together, yielding the composite step response shown in Fig. 10. The step response time constant  $\tau_s$  is defined as the rise time for the sensor to reach 63.2% of the steady-state voltage [13,26,46]. From Fig. 10, a time constant of 0.4 s  $\pm$  0.05 s is inferred for the TSE heat flux sensor. An identical result (not shown) was obtained by stepping the power down from 144 to 0 mW.

## 6.2. Amplitude-frequency response

The amplitude-frequency response (AFR) [24] of the TSE heat flux sensor was characterized. In this test, the response of the sensor is measured subject to sinusoidal heating conditions over a wide range of frequencies. The power output of the 808 nm diode laser was modulated as a sinusoidal waveform with a frequency adjusted from 0.01 to 20 Hz in discrete steps; for all frequencies, the optical power of the laser was maintained at a constant amplitude of 120 mW peak-to-peak. The amplitude of the TSE heat flux sensor's voltage signal at the frequency of the heat pulse was measured using a lock-in amplifier (Stanford Research Systems model SR810).

The AFR test results for the TSE heat flux sensor are shown in Fig. 11. The response amplitude is constant for heat pulse frequencies up to

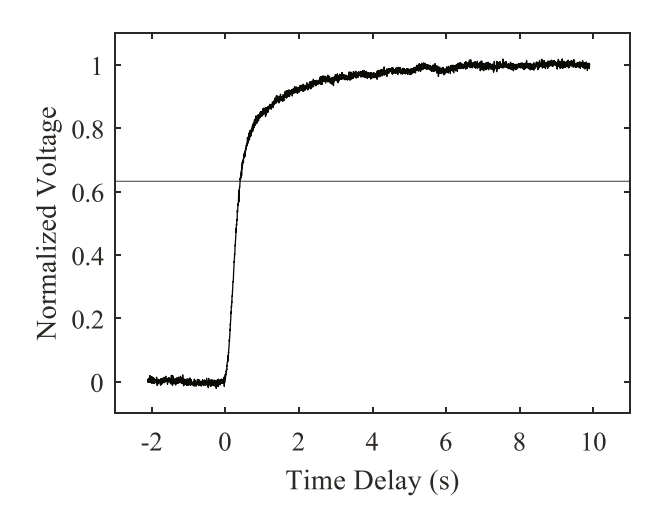


**Fig. 10.** Composite transient of the TSE heat flux sensor voltage output in response to a step heat flux. The data represent an average of 36 repeat transients. The horizontal line corresponds to 63.2% of the steady-state voltage.

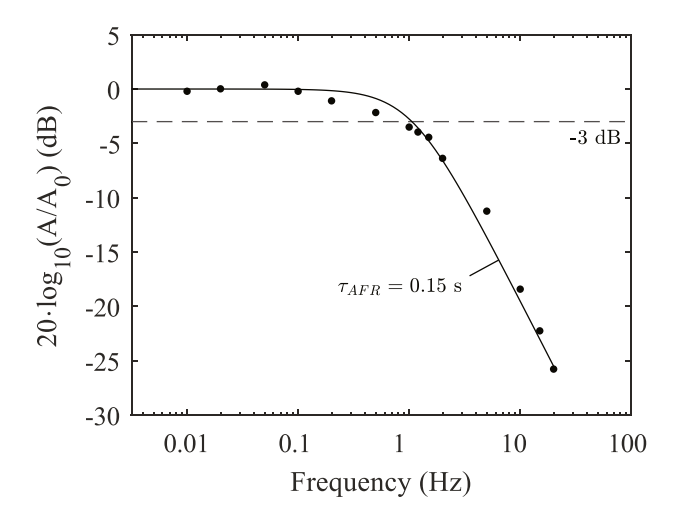


Fig. 11. Amplitude-frequency response of the TSE heat flux sensor. Voltage amplitudes A are normalized by the sensor's steady-state output voltage  $A_0$ . The line fit through the data represents a first-order response model with a time constant  $\tau_{AFR}$  of 0.15 s. The dashed line represents an attenuation of -3 dB.

0.1 Hz and is attenuated by -3 dB at a frequency between 0.5 and 1 Hz, decaying quickly thereafter. The AFR time constant  $\tau_{AFR}$  is determined by fitting the data using a first-order response model, for which the response amplitude A decays with increasing frequency according to Eq. (7) [24].

$$\frac{A}{A_0} = \frac{1}{\sqrt{1 + (2\pi f \tau_{AFR})^2}} \tag{7}$$

In Eq. (7), f is the frequency of the heat pulse waveform and  $A_0$  is the amplitude of the TSE heat flux sensor response in the limit of  $f \to 0$ . An AFR time constant of 0.15 s produces an optimal fit of Eq. (7) to the data in Fig. 11.

## 6.3. Analysis of the sensor's transient response

A prior TSE heat flux sensor that was fabricated in a similar configuration [15] had a time constant of 4.4 s, while the sensor reported

here is faster by an order of magnitude. The fast response time and high bandwidth of the current sensor is attributed to the placement of the transducers close to the surface of the sensor and elimination of any heat spreading components that were included on the prior TSE device.

Considering a transient response that is limited by the thermal inertia of the material in front of the transducers (here, an approximately 0.2 mm thick cement layer), the theoretical time constant of the TSE heat flux sensor for a step change in heat flux is predicted to be approximately 0.1 s [47]. This, however, does not consider heat conduction from the cement layer into the transducers, which will prolong the rise time of the sensor's response to steady-state conditions. Thus, a time constant of 0.1 s is considered a lower bound for the TSE heat flux sensor and in good qualitative agreement with the experimental results.

If a faster response time is desired, the thickness of the cement layer on the front face of the sensor can be reduced, or eliminated altogether. Without the coating layer, the transient response of the TSE heat flux sensor would become dominated by heat conduction within the rhenium transducers [47,48], and can result in a sensor with a time constant as low as 0.03 s. The coating, however, plays an important role protecting the transducer material from environmental effects (i.e. oxidation, sublimation, and erosion) that can reduce the sensor's lifespan. Thus, while fast response times can be achieved by tailoring the configuration of sensor components, it is important to consider the end-use case in the design.

#### 7. Sensor response to localized heating

The response of the TSE heat flux sensor at room temperature to a localized heat source was probed using a laser scanning technique. The localized heat source produces temperature gradients both normal and parallel to the front surface of the sensor to investigate the relative voltage contributions from the TSE and CSE [15]. An 808 nm continuous-wave diode laser (Thorlabs model L808P500MM) with an optical power of 119 mW and a focused 2 mm beam diameter was used as the heat source. The sensor was mounted to an automated translation stage. The laser was scanned at normal incidence across a  $12 \times 12$  mm area around the centroid of the heat flux sensor. The voltage output of the sensor was recorded for 576 discrete locations using a nanovoltmeter (Keithley model 2182).

The results of the laser scan experiment are shown in Fig. 12. Consistent with results from a prior TSE heat flux sensor [15], the scan produces a voltage profile characterized by alternating quadrants of high and low values superimposed over a positive voltage that decreases radially from the centroid (Fig. 12a). The extrema are positioned near the transducer and electrical wire junctions (Fig. 12b) and are driven by contributions from the CSE. The sign of the CSE contributions depends on the polarity of the junction (i.e., whether the electrical wire is oriented towards the positive or negative terminal of the nanovoltmeter), yielding the alternating high/low profile in Fig. 12a.

With the laser positioned over the centroid of the sensor, maximizing the TSE and minimizing the CSE, a voltage of 0.46  $\mu V$  was measured. This is a factor of 6 lower than the magnitude of the maximum and minimum voltage values at the extrema, 3.1 and  $-2.6 \mu V$ , respectively. By comparison, in the prior TSE heat flux sensor, the voltage was purely positive over the entire scan area, even at the local extrema [15]. There, the data suggested a sensor response that was dominated by the TSE, even when subject to heating conditions that were tailored to elicit a strong CSE contribution. In rhenium, the relatively low Seebeck coefficient anisotropy at room temperature renders the TSE comparatively smaller than the CSE. As such, these results highlight the importance of using at least two transducers arranged in series with 2-fold rotational symmetry (Fig. 9); when subject to a lateral temperature gradient that is uniform, the net contributions of the CSE to the output voltage are zero, even though CSE voltages at each junction may be significant [15]. With this configuration, only when non-uniform temperature gradients are present in the sensor, as was investigated in Section 5.1, do CSE voltages begin to contribute to the output voltage.

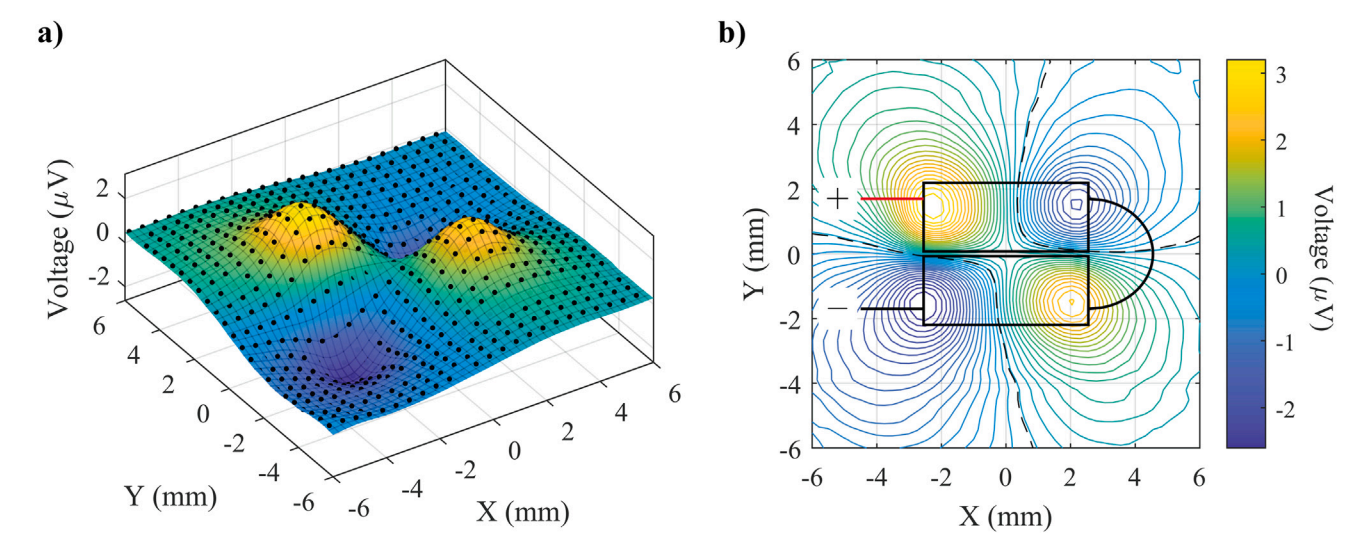


Fig. 12. Laser scan data. (a) Isometric view of the TSE heat flux sensor voltage output as a function of the position of the localized laser heat probe with respect to the centroid of the sensor. (b) Contour plot of the TSE heat flux sensor voltage output with the outline of the rhenium transducers and wiring overlaid on top of the data. The dashed contour lines represent a measured voltage of 0 V.

## 8. Conclusions

A high-temperature heat flux sensor was developed using the transverse Seebeck effect in single crystal rhenium. Among the elements, rhenium's high-temperature compatibility and extensive heritage in harsh environments render it a promising choice for TSE-based heat flux sensors tailored for aerospace and energy production applications. The sensor design utilizing the TSE and its rugged package contribute to its ability to survive temperatures of, at least, 1000 °C. The responsivity of the sensor is predicted to more than quintuple in magnitude from 25 °C to 1000 °C, owed to the unique temperature-dependent behavior of rhenium's Seebeck coefficient tensor components. The temperaturedependent responsivity of the sensor was characterized from room temperature to 500 °C and was found to be in good agreement with analytical predictions. Over repeat calibration sweeps, the sensor's responsivity demonstrated good reproducibility following an initial exposure to 500 °C, highlighting the stability of the sensor once properly cured at application-relevant temperatures. The sensor exhibits a time constant of 0.4 s when exposed to a step increase in heat flux and can resolve dynamic heating conditions with frequencies up to 0.1 Hz without attenuation of its output signal, adequate for resolving long time-scale transient heating phenomena during high-speed flight and dynamic energy production.

Due to the characteristics of the transverse Seebeck effect and the capabilities of rhenium, the sensor configuration demonstrated here can be adapted to elicit performance characteristics better tailored for mission requirements. For example, the thickness of the transducer and sensor package can be decreased to yield a faster response time without attenuation of the sensor's responsivity. If a higher operating temperature is desired, alternative ceramic materials, and of different form factors, can be used as packaging without modification to the heat flux-to-voltage transduction circuit, which is compatible with temperatures as high as 3000 °C. Overall, these results demonstrate the unique application of the TSE in refractory metal single crystals for heat flux sensing, and highlight the potential performance that can be achieved by these sensors in extreme environments.

#### CRediT authorship contribution statement

**Kenneth McAfee:** Writing – original draft, Visualization, Software, Methodology, Investigation, Formal analysis, Data curation. **Peter B. Sunderland:** Writing – review & editing, Visualization, Supervision,

Methodology, Funding acquisition, Conceptualization. **Oded Rabin:** Writing – review & editing, Visualization, Supervision, Project administration, Methodology, Funding acquisition, Conceptualization.

## **Declaration of competing interest**

The authors declare that they have no known competing financial interests or personal relationships that could have appeared to influence the work reported in this paper.

#### Acknowledgments

This work was supported by the U.S. Department of Energy, United States [grant DEFE0031902]. K.M. acknowledges support from NASA, United States [grant 80NSSC23K1201]. We thank Nolan Ballew and Dr. Don Schmadel for the fabrication of sensor components. We thank Prof. Gianna Valentino and Mr. Eliott Pierre-Cloud Wallace for technical assistance with high-temperature processing.

## Data availability

Data will be made available on request.

## References

- H.S. Alpert, D.A. Saunders, M. Mahzari, J.D. Monk, T.R. White, T.K. West, Inverse estimation and sensitivity analysis of Mars 2020 entry aeroheating environments, J. Spacecr. Rockets 60 (3) (2023) 899–911, http://dx.doi.org/10.2514/1.A35571.
- [2] B.W. Butler, B.W. Webb, Measurement of radiant heat flux and local particle and gas temperatures in a pulverized coal-fired utility-scale boiler, Energy Fuels 7 (6) (1993) 835–841, http://dx.doi.org/10.1021/ef00042a020.
- [3] Z. Li, J. Jing, G. Liu, Z. Chen, C. Liu, Measurement of gas species, temperatures, char burnout, and wall heat fluxes in a 200-MW<sub>e</sub> lignite-fired boiler at different loads, Appl. Energy 87 (4) (2010) 1217–1230, http://dx.doi.org/10.1016/j.apenergy.2009.05.035.
- [4] R.A. Miller, C.Y. Tang, J.A.B. Santos, T.R. White, B.A. Cruden, Aftbody heat flux measurements during Mars 2020 entry, J. Spacecr. Rockets 61 (2) (2024) 369–382, http://dx.doi.org/10.2514/1.A35783.
- [5] A. Gülhan, T. Thiele, F. Siebe, R. Kronen, Combined instrumentation package COMARS+ for the ExoMars Schiaparelli lander, Space Sci. Rev. 214 (1) (2018) 12, http://dx.doi.org/10.1007/s11214-017-0447-4.
- [6] L. Li, J. Wang, X. Fan, Development of integrated high temperature sensor for simultaneous measurement of wall heat flux and temperature, Rev. Sci. Instrum. 83 (7) (2012) 074901, http://dx.doi.org/10.1063/1.4731685.

- [7] R.A. Miller, H.S. Alpert, Temperature dependent performance of Schmidt–Boelter heat flux sensors, Rev. Sci. Instrum. 94 (2) (2023) 025002, http://dx.doi.org/ 10.1063/5.0129703.
- [8] A.R. Gifford, D.O. Hubble, C.A. Pullins, T.E. Diller, S.T. Huxtable, Durable heat flux sensor for extreme temperature and heat flux environments, J. Thermophys. Heat Transfer 24 (1) (2010) 69–76, http://dx.doi.org/10.2514/1.42298.
- [9] C.A. Pullins, T.E. Diller, In situ high temperature heat flux sensor calibration, Int. J. Heat Mass Transfer 53 (17–18) (2010) 3429–3438, http://dx.doi.org/10. 1016/j.ijheatmasstransfer.2010.03.042.
- [10] C.A. Pullins, T.E. Diller, Direct measurement of hot-wall heat flux, J. Ther-mophys. Heat Transfer 26 (3) (2012) 430–438, http://dx.doi.org/10.2514/1. T3772
- [11] J.R. Trelewicz, J.P. Longtin, C. Gouldstone, P.J. Kennedy, J.M. Donbar, Heat flux measurements in a scramjet combustor using embedded direct-write sensors, J. Propuls. Power 31 (4) (2015) 1003–1013, http://dx.doi.org/10.2514/1.B35585.
- [12] J.R. Trelewicz, J.P. Longtin, D.O. Hubble, R.J. Greenlaw, High-temperature calibration of direct write heat flux sensors from 25 °C to 860 °C using the in-cavity radiation method, IEEE Sensors J. 15 (1) (2015) 358–364, http://dx. doi.org/10.1109/JSEN.2014.2343931.
- [13] X. Li, L. Zhang, H. Xie, Z. Shang, X. Zhang, X. Qi, M. Lu, Q. Tan, Preparation and performance evaluation of a miniature high-temperature heat flux sensor with centralized thermal insulation structure, IEEE Trans. Instrum. Meas. 73 (2024) 1–8, http://dx.doi.org/10.1109/TIM.2024.3420362.
- [14] X. Fu, Q. Lin, Y. Peng, J. Liu, X. Yang, B. Zhu, J. Ouyang, Y. Zhang, L. Xu, S. Chen, High-temperature heat flux sensor based on tungsten-rhenium thin-film thermocouple, IEEE Sensors J. 20 (18) (2020) 10444–10452, http://dx.doi.org/10.1109/JSEN.2020.2993592.
- [15] K. McAfee, P.B. Sunderland, O. Rabin, A heat flux sensor leveraging the transverse seebeck effect in elemental antimony, Sensors Actuators A: Phys. 363 (2023) 114729, http://dx.doi.org/10.1016/j.sna.2023.114729.
- [16] T. Meier, P. Stathopoulos, P.R. Von Rohr, Design and convective calibration of a transverse heat flux sensor, Exp. Heat Transfer 29 (2) (2016) 139–150, http://dx.doi.org/10.1080/08916152.2014.945050.
- [17] Y. Huang, J. Yang, Y. Wang, B. Dai, Exploring the transverse thermoelectric effect of 4H-SiC single crystal for the applications of high-energy infrared laser detection, ACS Photonics 12 (4) (2025) 2106–2111, http://dx.doi.org/10.1021/ acsphotonics.4c02569.
- [18] X. Chen, B. Tao, R. Zhao, K. Yang, Z. Li, T. Xie, Y. Xia, Fast-response thin film heat flux sensors for harsh environments, IEEE Sensors J. 24 (12) (2024) 18844–18850, http://dx.doi.org/10.1109/JSEN.2024.3393775.
- [19] H.J. Goldsmid, Application of the transverse thermoelectric effects, J. Electron. Mater. 40 (5) (2011) 1254–1259, http://dx.doi.org/10.1007/s11664-010-1357-3.
- [20] Y. Tang, B. Cui, C. Zhou, M. Grayson, P x N-type transverse thermoelectrics: A novel type of thermal management material, J. Electron. Mater. 44 (6) (2015) 2095–2104, http://dx.doi.org/10.1007/s11664-015-3666-z.
- [21] K.F. Renk, J. Betz, S. Zeuner, H. Lengfellner, W. Prettl, Thermopile effect due to laser radiation heating in thin films of high- $T_c$  materials, Phys. C: Supercond. 235–240 (1994) 37–40, http://dx.doi.org/10.1016/0921-4534(94)91308-0.
- [22] H. Lengfellner, G. Kremb, A. Schnellbögl, J. Betz, K.F. Renk, W. Prettl, Giant voltages upon surface heating in normal YBa $_2$ Cu $_3$ O $_{7-\delta}$  films suggesting an atomic layer thermopile, Appl. Phys. Lett. 60 (4) (1992) 501–503, http://dx.doi.org/10. 1063/1.106613.
- [23] T. Roediger, H. Knauss, U. Gaisbauer, E. Kraemer, S. Jenkins, J. Von Wolfersdorf, Time-resolved heat transfer measurements on the tip wall of a ribbed channel using a novel heat flux sensor—Part I: sensor and benchmarks, J. Turbomach. 130 (1) (2008) 011018, http://dx.doi.org/10.1115/1.2751141.
- [24] H. Knauss, T. Roediger, D.A. Bountin, B.V. Smorodsky, A.A. Maslov, J. Srulijes, Novel sensor for fast heat flux measurements, J. Spacecr. Rockets 46 (2) (2009) 255–265, http://dx.doi.org/10.2514/1.32011.
- [25] K. Huber, F. Gackstatter, T. Rödiger, M. Wensing, Highly time-resolved heat flux measurement in a combustion engine, Int. J. Engine Res. 24 (6) (2023) 2338–2351, http://dx.doi.org/10.1177/14680874221118970.
- [26] S. Song, Y. Wang, L. Yu, Highly sensitive heat flux sensor based on the transverse thermoelectric effect of  $YBa_2Cu_3O_{7-\delta}$  thin film, Appl. Phys. Lett. 117 (12) (2020) http://dx.doi.org/10.1063/5.0021451.
- [27] X. Chen, B. Tao, R. Zhao, K. Yang, Z. Li, T. Xie, Y. Zhong, T. Zhang, Y. Xia, The atomic layer thermopile heat flux sensor based on the inclined epitaxial  $YBa_2Cu_3O_{7-\delta}$  films, Mater. Lett. 330 (2023) 133336, http://dx.doi.org/10.1016/j.matlet.2022.133336.

- [28] P.G. Huggard, S. Zeuner, K. Goller, H. Lengfellner, W. Prettl, Normal state  $YBa_2Cu_3O_x$  films: A new fast thermal detector for far infrared laser radiation with a uniform wavelength response, J. Appl. Phys. 75 (1) (1994) 616–618, http://dx.doi.org/10.1063/1.355795.
- [29] K. Takahashi, T. Kanno, A. Sakai, H. Adachi, Y. Yamada, Gigantic transverse voltage induced via off-diagonal thermoelectric effect in Ca<sub>x</sub>CoO<sub>2</sub> thin films, Appl. Phys. Lett. 97 (2) (2010) 021906, http://dx.doi.org/10.1063/1.3464286.
- [30] K. Takahashi, A. Sakai, T. Kanno, H. Adachi, Tailoring of inclined crystal orientation in layered cobaltite thin films for the development of off-diagonal thermoelectric effect, Appl. Phys. Lett. 95 (5) (2009) 051913, http://dx.doi.org/ 10.1063/1.3194796.
- [31] G. Yang, L. Zhang, Laser induced thermoelectric voltage effect of Bi<sub>2.1</sub>Sr<sub>1.9</sub>CaCu<sub>2</sub>O<sub>8</sub> thin films, in: International Photonics and OptoElectronics Meetings (2014), Paper JF2A.41, Optica Publishing Group, 2014, p. JF2A.41, http://dx.doi.org/10.1364/FBTA.2014.JF2A.41.
- [32] A.V. Mityakov, S.Z. Sapozhnikov, V.Y. Mityakov, A.A. Snarskii, M.I. Zhenirovsky, J.J. Pyrhönen, Gradient heat flux sensors for high temperature environments, Sensors Actuators A: Phys. 176 (2012) 1–9, http://dx.doi.org/10.1016/j.sna. 2011.12.020.
- [33] F. Janasz, H.-M. Prasser, D. Suckow, A. Mityakov, The use of a novel gradient heat flux sensor for characterization of reflux condensation, Nucl. Eng. Des. 395 (2022) 111885, http://dx.doi.org/10.1016/j.nucengdes.2022.111885.
- [34] S.Z. Sapozhnikov, V.Y. Mityakov, A.V. Mityakov, Bismuth-based gradient heat-flux sensors in thermal experiment, High Temp. 42 (4) (2004) 629–638, http://dx.doi.org/10.1023/B:HITE.0000039993.76288.01.
- [35] L.A. Konopko, A.A. Nikolaeva, A.K. Kobylianskaya, T.E. Huber, Anisotropic thermoelectric devices made from single-crystal semimetal microwires in glass coating, J. Electron. Mater. 47 (6) (2018) 3171–3176, http://dx.doi.org/10. 1007/s11664-018-6272-z.
- [36] Z. Liu, S. Liu, J. Zhao, Y. Yue, Q. Xu, F. Yang, A transient heat flux sensor based on the transverse seebeck effect of single crystal Bi<sub>2</sub>Te<sub>3</sub>, Measurement 198 (2022) 111419, http://dx.doi.org/10.1016/j.measurement.2022.111419.
- [37] T. Xie, B. Tao, R. Zhao, X. Chen, Z. Li, M. Zhao, W. Chen, Exploration of the transverse seebeck effect in the inclined nitrogen-doped 4H-SiC thin film, Measurement 243 (2025) 116459, http://dx.doi.org/10.1016/j.measurement.2024. 116459.
- [38] V. Zinov'ev, P. Gel'd, S. Il'inykh, V. Sperelup, N. Korenovskij, Anisotropy of Re kinetic properties at high temperatures, Teplofiz. Vys. Temp. 20 (3) (1982) 481–485.
- [39] T. Kanno, K. Takahashi, A. Sakai, H. Tamaki, H. Kusada, Y. Yamada, Detection of thermal radiation, sensing of heat flux, and recovery of waste heat by the transverse thermoelectric effect, J. Electron. Mater. 43 (6) (2014) 2072–2080, http://dx.doi.org/10.1007/s11664-013-2959-3.
- [40] A.T. Burkov, M.V. Vedernikov, High-temperature thermoelectric power and electrical resistivity of single-crystal rhenium and their relation with the electronic structure, J. Exp. Theor. Phys. 85 (1983) 1821–1825.
- [41] C.Y. Ho, R.W. Powell, P.E. Liley, Thermal conductivity of the elements, J. Phys. Chem. Ref. Data 1 (2) (1972) 279–421, http://dx.doi.org/10.1063/1.3253100.
- [42] A.T. Burkov, A. Heinrich, P.P. Konstantinov, T. Nakama, K. Yagasaki, Experimental set-up for thermopower and resistivity measurements at 100-1300 K, Meas. Sci. Technol. 12 (3) (2001) 264–272, http://dx.doi.org/10.1088/0957-0233/12/3/304.
- [43] K. McAfee, Heat Flux Sensors and Reconstruction Techniques for Atmospheric Entry Spacecraft (Ph.D. thesis), University of Maryland, 2025, URL http://hdl. handle.net/1903/3.
- [44] W.M. Pitts, A.V. Murthy, J.L. de Ris, J.-R. Filtz, K. Nygård, D. Smith, I. Wetterlund, Round robin study of total heat flux gauge calibration at fire laboratories, Fire Saf. J. 41 (6) (2006) 459–475, http://dx.doi.org/10.1016/j.firesaf.2006.04.004.
- [45] A. Murthy, B. Tsai, R. Saunders, Radiative calibration of heat-flux sensors at NIST: facilities and techniques, J. Res. Natl. Inst. Stand. Technol. 105 (2) (2000) 293, http://dx.doi.org/10.6028/jres.105.033.
- [46] Heat flux transducers and infrared radiometers for the direct measurement of heat transfer rates, MEDTHERM Corp. Bull. 118 (2003).
- [47] N.E. Hager, Thin foil heat meter, Rev. Sci. Instrum. 36 (11) (1965) 1564–1570, http://dx.doi.org/10.1063/1.1719394.
- [48] S. Zeuner, H. Lengfellner, W. Prettl, Thermal boundary resistance and diffusivity for  $YBa_2Cu_3O_{7-\delta}$  films, Phys. Rev. B 51 (17) (1995) 11903–11908, http://dx.doi.org/10.1103/PhysRevB.51.11903.